The microwave-assisted synthesis of P2 and O3 type Na<sub>x</sub>CoO<sub>2</sub> cathode materials studied by in situ Raman spectroscopy

John Jamboretz<sup>a</sup>, Yuwei Zhu<sup>b</sup>, Rylee James<sup>a</sup>, Linqin Mu<sup>b</sup>, \*Christina S. Birkel<sup>a,c</sup>

<sup>a</sup> School of Molecular Sciences, Arizona State University, Tempe, 85287, AZ, USA

<sup>b</sup> School of Engineering for Matter, Transport, and Energy, Arizona State University, Tempe,

85287, AZ, USA

<sup>c</sup> Department of Chemistry and Biochemistry, Technische Universität Darmstadt, 64287

Darmstadt, Germany

**ABSTRACT** 

A microwave heating protocol was developed for the rapid preparation of two polytypes of Na<sub>x</sub>CoO<sub>2</sub> with distinct crystal structures. Two methods using conventional furnace heating with different heating rates were also developed to study the effects of heating rate and microwave irradiation on the formation pathway and final products. Both O3 type NaCoO<sub>2</sub> and P2 type Na<sub>0.68-0.76</sub>CoO<sub>2</sub> were prepared by heating a mixture of Na<sub>2</sub>O<sub>2</sub> and Co<sub>3</sub>O<sub>4</sub> to 850 °C followed by immediate cooling. Adjusting the Na precursor ratio selectively targeted the two phases. In order to compare the formation pathway, intermediate species obtained after the first reaction

occurring at around 350 °C were identified by ex situ X-ray diffraction and in situ Raman spectroscopy. A mixture of Na<sub>x</sub>CoO<sub>2</sub> phases was found, showing rapid formation at this temperature, consistent with previous in situ studies. Higher heating rates increased the peak reaction temperature, accelerating reaction completion and increasing intermediate crystallite size. However, the final product's composition, structure, and morphology were unaffected by the heating method. Electrochemical performance in coin cells showed that all O3 and P2 type products had slightly lower initial capacity compared to previous reports but did not vary significantly between heating methods. Capacity retention over 100 cycles was stable for the O3 phase but showed dramatic reduction for the P2 phase in all heating methods. This study demonstrates a promising rapid synthesis method that could promote the commercialization of Na-containing layered cathode materials.

### INTRODUCTION

Layered Na<sub>x</sub> $MO_2$  (M = transition metals) compounds have been widely investigated as potential positive cathode materials for sodium ion batteries (SIBs). They continue to receive significant attention for their potential application in large scale energy storage because of the use of earth abundant Na over limited Li supplies. Recent research progress and performance metrics have been extensively reviewed, howing they possess good promise in commercial applications. The crystal structures within this family share a common layered motif with a single layer plane of octahedral metal oxide and a single layer of Na ions. Orientation and alignment of the metal oxide layers provide a different Na coordination environment, summarized by Delmas notation, where O = octahedral and O = octahedral

Jahn-Teller distortion or Na vacancy ordering. The arrangement has critical impact on important performance parameters for SIBs, including energy density, cycle life, and stability.<sup>6</sup>

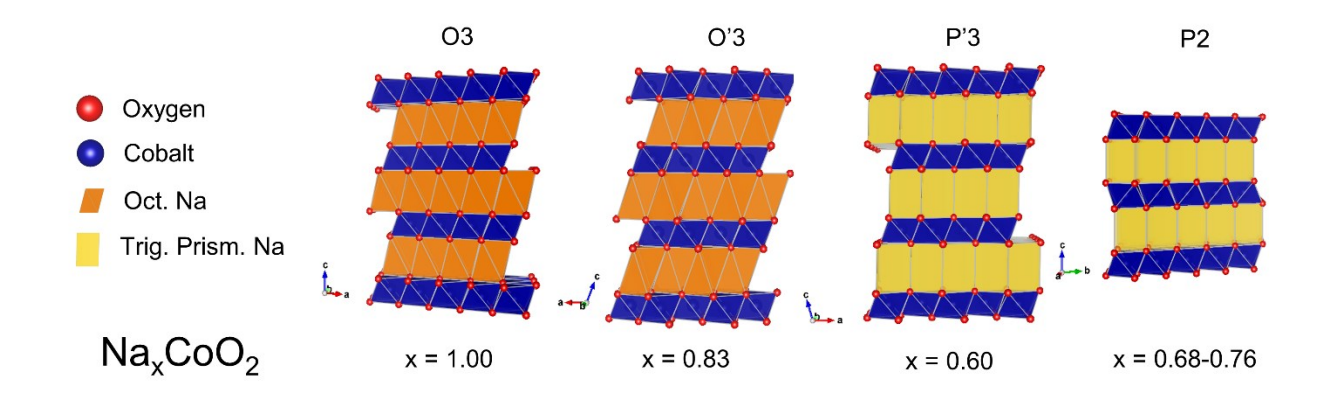


Figure 1: Crystal structures of the four Na<sub>x</sub>CoO<sub>2</sub> phases, viewed down the b (a) direction for the 3-layer (2-layer) phases.

Table 1: Summary of the several different crystal structures for Na<sub>x</sub>CoO<sub>2</sub> compounds synthesized through solid-state methods reported by Lei *et al.*<sup>7</sup> They are heated at a rate of 5 °C/min and held for 16 hours at temperature under air (or oxygen for O3) atmosphere followed by quenching in air.

	Na <sub>1.00</sub> CoO2	Na <sub>0.83</sub> CoO2	Na <sub>0.60</sub> CoO2	Na <sub>0.68-0.76</sub> CoO2
Delmas notation	О3	O'3	P'3	P2
Crystal system	trigonal	monoclinic	monoclinic	hexagonal
Space group	R3m (166)	C2/m (12)	C2/m (12)	$P6_3/mmc$ (194)
Synthesis temperature	450 °C	650 °C	535 °C	750 °C
$Na_2O_2$ : $Co_3O_4$ ratio:	Na:Co = 1.05	Na:Co = 1.00	Na:Co = 0.68	Na:Co = 0.68-0.76

Na<sub>x</sub>CoO<sub>2</sub> was the first of this family to be investigated for SIB commercialization.<sup>1</sup> It exhibits a 2-layer polytype P2 – Na<sub>0.68-0.76</sub>CoO<sub>2</sub> which is obtained by direct solid-state synthesis in a slightly variable Na stoichiometry and several 3-layer polytypes O3, O'3, P'3 obtained at finite Na stoichiometries (Figure 1). During Na addition/removal by chemical or electrochemical means, the 3-layer polytypes undergo phase transitions between the 3-layer structures listed here and another P3 structure not obtainable by direct synthesis.<sup>7</sup> The P2 phase conversely retains its structure during charging and discharging.<sup>8</sup> Direct syntheses of these phases are achievable by typical solid-state methods, but proper selection of reactants, stoichiometry, temperature, and time

are essential to isolate them as single phases. These have been summarized by Lei *et al.*<sup>7</sup> (Table 1) with their determination of single phase regions in the initial Na:Co ratio and temperature phase diagram. The reaction pathway for the P2 phase synthesis has been recently studied using in situ X-ray powder diffraction by Bianchini *et al.*,<sup>9</sup> observing that the O3 phase forms first and rapidly when Na<sub>2</sub>O<sub>2</sub> is used. Subsequent transitions to O'3 then P'3 with fast kinetics were observed with increasing temperature. The fast kinetics of the conversions between the 3-layer polytypes is attributed to fast Na ion diffusion and facile CoO<sub>6</sub> layer-gliding mechanism. Finally, an irreversible transition to the P2 phase was observed with slow kinetics, requiring a significant increase in temperature to complete. The necessity of elevated temperature to complete the conversion from 3-layer to 2-layer form is attributed to the requirement to reform Co-O bonds. The study indicated the process proceeds through a nucleation and growth mechanism guided by Johnson-Mehl-Avrami-Kolmogorov (JMAK) kinetics.

Microwave (MW)-assisted synthesis of inorganic compounds is an attractive time and energy-reducing method for obtaining fast-forming and potentially metastable materials as it exhibits rapid and volumetric heating.<sup>10–12</sup> Since the inception of using microwaves to heat foods in the 1950's, the technique has been extended to industrial applications for drying of commercial products, degradation of environmental contaminants, vulcanization and polymerization, and ceramics and metallics sintering, primarily due to the ability of microwave energy to heat internally and selectively.<sup>13</sup> Microwave heating has remained an academic interest for inorganic materials preparations. The interest began in 1988 when Baghurst and Mingos recognized that certain metal oxides could be heated directly by microwave irradiation and induce desired reactions.<sup>14</sup> Since then, the method has been demonstrated for obtaining a wide range of materials including carbides (e.g. SiC, (V/Cr)<sub>2</sub>GeC, V<sub>4</sub>AlC<sub>3</sub>), chalcogenides (e.g. PbSe, ZnS) and oxides (e.g. CuFe<sub>2</sub>O<sub>4</sub>), <sup>14–26</sup>

often with dramatic reduction in necessary synthesis time. The interaction between reactants and microwave radiation leads to direct heating of the precursors internally which will impact the synthesis process and final products. In general, the differences between MW and conventional (furnace) heating have not been well investigated in the solid-state syntheses of inorganic materials, and only a limited number of studies using in situ analytical methods exist. <sup>27–32</sup> Recently, our group has developed an in situ Raman spectroscopy instrument for tracking phase changes during MW heating at high temperatures monitoring the structural change from anatase to rutile TiO<sub>2</sub> as a model system. <sup>33</sup>

Here, we successfully synthesized P2-Na<sub>0.68-0.76</sub>CoO<sub>2</sub> and O3-NaCoO<sub>2</sub> materials through rapid MW heating in high crystalline purity. To investigate potential impacts of microwave irradiation itself on the synthesis of Na<sub>x</sub>CoO<sub>2</sub>, a method of rapid conventional heating by use of a preheated furnace was also developed. Rapid heating rates similar to those encountered during MW heating were achieved. These were compared to a conventional furnace heating method where a slower heating rate was used which allowed the separation of heating rate and microwave irradiation effects. To compare the products (and their formation pathway) obtained by MW heating and furnace heating, their composition, structure, and morphology were investigated by X-ray powder diffraction, electron microscopy and Raman spectroscopy (ex situ and in situ). Finally, the cathode performance in Na battery cells was assessed, showing comparable capacity and cyclability to those previously reported for O3<sup>34</sup> and P2<sup>35</sup> phase by each method developed. Our findings unveil a promising synthesis technique by microwave heating that is both rapid and energy-efficient, offering a readily applicable solution for a variety of material systems in energy storage devices.

#### **EXPERIMENTAL**

The layered compounds were synthesized from Co<sub>3</sub>O<sub>4</sub> (Thermo Scientific, 99%) and Na<sub>2</sub>O<sub>2</sub> (Sigma Aldrich, 97%). A Retsch MM 400 shaker mill was used to homogenize starting materials using an airtight 25 ml tungsten carbide container (53 mm height, 22 mm diameter; Teflon gasket) and two 15 mm diameter tungsten carbide balls. Filling and emptying of the airtight mill container were performed in an Ar-filled glove box. The Na<sub>2</sub>O<sub>2</sub> granules were initially reduced to a powder by ball milling for 5 minutes at 20 cycles/s. Starting material powder was then prepared at a 10-gram scale using the appropriate stoichiometric ratios and milled for 90 minutes at 20 cycles/s. The ratios utilized for each heating method are presented in the main text (Table 3). Finally, 0.45 g pellets were prepared by pressing in a 13 mm diameter die (Stainless steel, Specac) at 1 ton for at least 10 seconds under Argon. Pellets were placed in individual vials and sealed with parafilm before removing them from the glove box until immediate use to prevent moisture exposure of the Na<sub>2</sub>O<sub>2</sub>.

Furnace methods utilized a Minithal 31 (Kanthal) small vertical tube furnace. The samples were heated in a 10 ml alumina crucible (AL-1010, Advalue Technology) that was supported just above the center of the furnace. We employed two different heating methods with the furnace, slow furnace (SF) and fast furnace (FF), (see Table 3) to investigate the effects of heating rate on the reaction outcome. For SF methods, the pellet was added to a preheated crucible within the furnace set at 100 °C. The temperature was increased at a fixed rate of 25 °C/min until the target temperature was reached (as measured by optical pyrometer, for details see below). For FF methods, the furnace was preheated to 1200 °C. Then the crucible with sample pellet was placed quickly inside and allowed to heat to the target temperature. For microwave (MW) methods, the 10 ml "sample-containing" alumina crucible (AL-1010, Advalue Technology) was nested inside a larger 20 ml "susceptor-containing" alumina crucible (AL-1020, Advalue Technology) containing

20 g of Fe<sub>3</sub>O<sub>4</sub> (natural, 94%, Alpha Chemicals) susceptor. This was kept at 100 °C until just before use. Then the sample pellet was added and immediately heated in a multimode microwave reactor operating at 2.45 GHz (CEM, Mars 6 Synthesis). The constant power level was 900 W for the O3 synthesis and 1500 W for the P2 synthesis. The power was turned off once the target temperature was reached. In all heating methods the sample was either allowed to cool naturally to 100-200 °C for final products or quenched for intermediates then immediately transferred to an Ar-filled glovebox. The samples were then gently ground with an agate mortar before analysis. Intermediates were obtained by quenching the samples immediately following the observation of a large temperature spike just after reaching >350 °C. After the temperature receded following this spike, upon the first observation of the temperature beginning to rise again the sample was quickly removed and quenched on Al foil. All methods were performed within the microwave reactor chamber with identical air ventilation rates.

Powder X-ray diffraction (XRD) measurements were performed on a STOE STADI P instrument in transmission geometry using Mo K- $\alpha$ 1 ( $\lambda$  = 0.709260 Å) radiation. Samples were pressed between two Mylar films and loaded onto disc shaped holders with 3 mm diameter apertures. Measurements were taken in a 2-51.23° 2 $\theta$  range with a 1° step size and 70 s/step using a linear position-sensitive detector covering 18.6° 2 $\theta$  range, giving a total measurement time of 1260 seconds per step. Measurements were 60 minutes.

Rietveld refinements of the XRD data were performed in TOPAS.<sup>36</sup> For all phases, scale and lattice parameters were refined. A phase was removed from the analysis if its weight percent was less than 1%. Size was refined using a single Voigt profile for major phases and the resulting integral breadth of the volume weighted mean column length distribution (IB-L<sub>vol</sub>) is reported if refined (SI C). For P2-Na<sub>x</sub>CoO<sub>2</sub>, a value of x = 0.72 for the Na site occupancies was fixed and not refined.

Scanning electron microscopy (SEM) measurements were performed on a Zeiss Auriga microscope. A small amount of each product was distributed on carbon tape inside an Ar-filled glovebox to prepare for measurements. These were transported in a sealed container on activated 3 Å molecular sieves until just before loading the instrument to minimize moisture exposure. Images were collected using 5 kV electron beam energy.

Raman measurements were performed with a custom-built system as described elsewhere,<sup>32</sup> with some modifications (SI E). A 532 nm CW laser (Hübner Photonics, Samba 100) operating at 30 mW was used for excitation. The minimum spot size on the sample is approximately 31 μm. The collections were performed in a 180 ° backscattering configuration. The spectrometer (Teledyne Princeton Instruments, FER-SCI-1024B X-VR) was equipped with 1024 x 256 (w. by h.) pixel back-illuminated CCD detector cooled to -55 °C and a 2400 g/mm grating (Teledyne Princeton Instruments, ISO81-GRT-2400-500) providing a pixel spacing of ~2 cm<sup>-1</sup>. Calibration was performed using a Hg atomic emission lamp. Sequential exposures of 0.979 s each are collected at a constant rate of 1 Hz.

Room temperature measurements of the products were performed on pressed powder of the products in a pellet die using the minimum registerable pressure (~0.1 ton). In these measurements, autofocus was not utilized. 100 sequential spectra were collected and averaged to obtain the final spectrum. In situ measurements were performed on the synthesis of two additional samples each of O3 and P2 by the SF and MW heating methods. Sequential spectra were collected until the synthesis was complete. In the furnace methods, temperature data were collected using a fine 0.1 mm diameter thermocouple (Omega, Type K, TJ36-CAXL-010U-25) pressed to the top surface of the sample pellet. Automated adjustment of the probe-to-sample distance ("autofocus") was applied to maintain focus throughout the synthesis. The sampling area was continuously moved in

an orbital raster pattern to reduce laser heating effects and provide a more representative bulk analysis of the sample surface. These are described in SI E.

Line profile analysis to extract the Raman peak shapes from room temperature Raman spectra was performed in TOPAS.<sup>36</sup> Instrument related broadening was first determined using a Hg emission line (546.1253 nm, 486.1754 relative cm<sup>-1</sup> from 532 nm excitation source) measured through the Raman probe. A natural Lorentzian line width of 1 cm<sup>-1</sup> was assumed for the emission line and convoluted with a gaussian profile to model the instrumental broadening. The fit gaussian width was taken to be the instrument related broadening and was used to deconvolute the collected Raman spectra. The broadening was assumed constant over the wavenumber range measured. Raman peaks were modelled as split pseudo-Voigt profiles. The full-width at half-maximum (FWHM) reported for the Raman peaks are the sum of the two half pseudo-Voigt profiles and the Lorentzian contribution is the average of the two.

Temperature was measured during synthesis by optical pyrometer (Optris, OPTCTL, 3MH3-CF4-CB3HC) with a spot size of 1.5 mm diameter at a focal length of 450 mm. The pyrometer was manually aligned using the built-in sight lasers to the center of the top surface of the sample pellet. Emissivity was fixed at 0.9 for all measurements. It is capable of temperature measurements >250 °C. Measurements were collected at a rate of 1 Hz.

To prepare cathode electrodes, a slurry comprising of the cathode material (85 wt%), acetylene black (10 wt%), and polyvinylidene fluoride (PVDF, 5 wt%) in 450 µl of N-methyl-2-pyrrolidone (NMP) solvent was prepared in a total slurry mass of 0.3 g. This was uniformly spread using the FlackTek SpeedMixer. The slurry was subsequently coated onto an Al foil with a Doctor Blade and dried at 60 °C under atmospheric conditions for 20 minutes. Following this, it underwent a 12-

hour vacuum drying at 110 °C to ensure complete removal of the NMP solvent. Then, the cathode electrode was punched into discs with a diameter of 12 mm and then transferred into an Ar-filled glove box immediately. A total of 3 measurements for each phase and preparation method were collected to characterize the repeatability of the measurements.

Coin cells (CR2032) were assembled inside an argon-filled glove box for electrochemical testing. We used the cathode disc as the positive side, the sodium metal chip as the negative electrode, 0.5 M NaClO<sub>4</sub> (98%, Sigma-Aldrich) dissolved in propylene carbonate as the electrolyte, and glass fiber as the separator. Then, all the battery tests were conducted using a Landt battery cycler within the voltage range of 2.0–4.0 V at ambient temperature.

#### RESULTS AND DISCUSSION

Three heating method protocols were developed to synthesize either O3 type NaCoO<sub>2</sub> and P2 type Na<sub>0.68-0.76</sub>CoO<sub>2</sub> which were targeted using two initial Na:Co precursor ratios, namely 1.05-1.10:1 for O3 phase and 0.75-0.80:1 for P2 phase. The three methods – slow furnace (SF), fast furnace (FF), and microwave (MW) – are distinguished by their heating rate and inclusion of microwave irradiation and are summarized in Table 3. A main conclusion is that the absolute maximum temperature reached is the crucial parameter to achieve complete reaction to phase pure products by all methods. Surprisingly, the optimal reaction temperature was found to be 850 °C for both O3 and P2 types (SI F Figure S23 and S24, respectively), in contrast to previously reported methods of obtaining O3 type at significantly lower temperature than P2 type.<sup>7</sup> Synthesis at lower temperature shows impurities consistent with incomplete reaction, i.e. O'3 phase in the O3 synthesis and P'3 phase in the P2 synthesis. For the microwave heating method, it was found that a higher power level of 1500 W was necessary to reach this temperature in the P2 synthesis

whereas in the O3 synthesis only 900 W was needed. It is speculated that this is due to the presence of excess Na phase, likely as  $Na_2O$ , in the O3 heating process (initial Na:Co ratio = 1.05:1) which may be heated directly by the microwave irradiation and result in higher temperatures achieved with lower power levels.

X-ray powder diffraction analysis of the O3 and P2 type oxides synthesized by the three different methods are shown in Figure 2. In all cases, the target compounds are constituted of the main phase with a weight percent of >96 wt% in all samples except for the O3 phase synthesized by MW heating which was obtained at 89 wt%. Rietveld refinements and all crystallographic data are compiled in the SI (SI C, Figures S3-14, Tables S3-14). The refined lattice parameters of the final products (Table 2) are in excellent agreement with those reported by Lei et al. <sup>7</sup> demonstrating the high quality of the products obtained from our methods comparable to those prepared by traditional solid-state synthesis methods. The MW synthesized O3 product showed the lowest purity with 89% weight. Interestingly, this MW O3 final product showed essentially no increase in O3 fraction relative to a quenched intermediate taken just after initial reaction of the precursors with an 88% weight O3 phase (SIC Table S3 and S9, final product and intermediate, respectively), in contrast with the other FF and SF products of an increase relative to the intermediates. The reason for this phenomenon remains unknown, but it could be attributed to the faster heating rate of the MW method which reduces the overall time at high temperatures and may not allow sufficient time for complete conversion to the O3 phase. Identified side phases are O'3 and Na<sub>2</sub>CO<sub>3</sub> for both the O3 and P2 syntheses. The small amount of Na<sub>2</sub>CO<sub>3</sub> is well explained by the reaction of Na<sub>2</sub>O (produced upon decomposition of the Na<sub>2</sub>O<sub>2</sub> precursor) with atmospheric CO<sub>2</sub> due to the ambient air conditions. The presence of O'3 in both the O3 and P2 products is better understood by examination of the reaction intermediates which were quenched from varied temperatures lower

than the target temperature (SI A, Table S1). In all cases, these were a varied mixture of some or all the phases (O3, O'3, P'3, P2). The small amount of O'3 remaining in the O3 product is likely due to incomplete diffusion of Na into the O'3/P'3 phases which may be present. The interconversion between 3-layer phases (O3, O'3, P'3) has low kinetic restriction as Na diffusion rates are high and the transition proceeds by simple layer gliding of the CoO<sub>6</sub> octahedra planes.<sup>9</sup> Conversely, the P2 phase has been shown to transition from any of the 3-layer parent phases (O3, O'3, or P'3) by a nucleation-growth mechanism. This has high kinetic restriction due to the need to break Co-O bonds to accomplish the structural change.<sup>9</sup> This suggests incomplete nucleation and propagation of P2 grains within the O'3 parent phases in the rapid synthesis methods presented here.

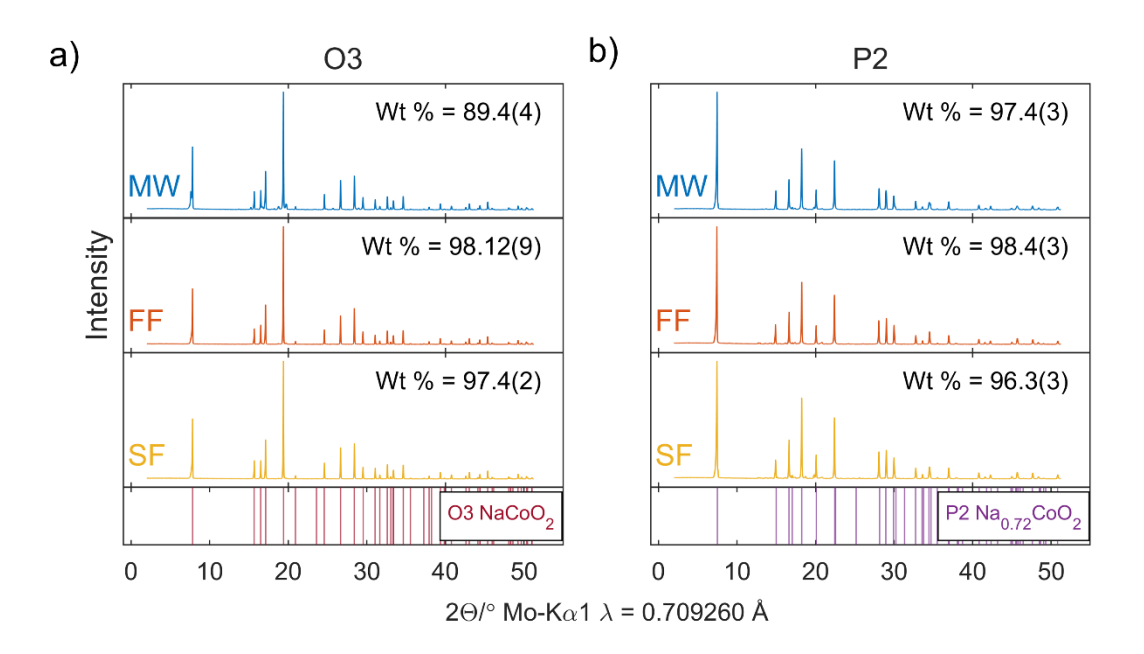


Figure 2: X-ray diffraction analysis of O3 NaCoO<sub>2</sub> (a) and P2 Na<sub>0.72</sub>CoO<sub>2</sub> (b) synthesized by the microwave (MW), fast furnace (FF) and slow furnace (SF) method, respectively. Refined weight percentages of the respective major phase are included (obtained by Rietveld refinement of the data, see SI C, Figure S3-14, Table S3-14). Below the diffractograms are reflection markers for the target phases of O3<sup>37</sup> (a) and P2<sup>38</sup> (b) In the MW O3 sample, splitting of the first peak (003) and the unmarked peaks are due to the presence of significant O'3 phase impurity as indicated by the Rietveld refinement analysis (SI C, Figure S3, Table S3).

Table 2: Lattice parameters reported by Lei *et al.*<sup>7</sup> and those determined by Rietveld refinement analysis of the final products in this study (SI C, Figure S3-14, Table S3-14). Values in parentheses are the standard errors for the last decimal reported. For the P2 samples, an x = 0.72 was assumed in the refinement.

	Literature	MW	FF	SF
O3-NaCoO <sub>2</sub>	a = 2.8883 c = 15.6019	a = 2.88950(3) c = 15.6035(3)	a = 2.89047(2) c = 15.6078(2)	a = 2.8896(2) c = 15.6033(2)
$P2-Na_xCoO_2$ x = 0.68-0.76	(x = 0.68) a = 2.8320 c = 10.8971	(x = 0.72) a = 2.83445(4) c = 10.9130(3)	(x = 0.72) a = 2.83120(4) c = 10.9441(2)	(x = 0.72) a = 2.83233(4) c = 10.9316(2)
	(x = 0.76) a = 2.8381 c = 10.8265			

Table 3: Description of the method and the average heating and cooling rates for each method, determined through temperature profiles, and Na:Co elemental ratio in precursor mixture of Na<sub>2</sub>O<sub>2</sub> and Co<sub>3</sub>O<sub>4</sub>.

	Slow furnace	Fast furnace	Microwave
Heating methods	(SF)	(FF)	(MW)
Methodology description	The sample is heated at the typical maximum heating rate for a conventional furnace to the target temperature	The sample is added to a preheated furnace to achieve high heating rates	The sample is heated rapidly by microwave irradiation and by a susceptor surrounding the sample
Heating rate	~20 °C/min	~50-100 °C/min	~100-200 °C/min
Cooling rate	~20 °C/min	~20 °C/min	~50 °C/min
Na:Co precursor ratio	P2 = 0.80:1	P2 = 0.75:1	P2 = 0.75:1
	O3 = 1.10:1	O3 = 1.05:1	O3 = 1.05:1

Detailed heating profiles of each method were collected using an optical pyrometer focused on the surface of the sample (Figure 3). A feature in the heating profile that is present in each method is a large spike in temperature which occurs once the temperature reaches around 350 °C. This spike is attributed to the exothermic decomposition of Na<sub>2</sub>O<sub>2</sub> followed by immediate reaction of the produced Na/Na<sub>2</sub>O and the precursor Co<sub>3</sub>O<sub>4</sub> to form an initial mixture of Na<sub>x</sub>CoO<sub>2</sub> phases. This is confirmed by in situ Raman data (Figure 6) and ex situ XRD analysis of intermediate compounds which were quenched immediately following the temperature spike (SI C, Figure S9-14). All quenched samples contained a mixture of the phases with the majority phase being O3, regardless of initial precursor Na:Co stoichiometry (Table 4). This is in good agreement with the observation of Bianchini et al. 9 that O3 phase is formed first from the precursor mixture at 364 °C and the reaction is completed rapidly within ~75 seconds. Interestingly, the temperature spike is consistently larger in the P2 synthesis despite the smaller amount of Na<sub>2</sub>O<sub>2</sub> utilized relative to the O3 synthesis. The origin of this is unknown; as the time scale of the temperature spike is very short, it may be a result of faster heat conduction of the P2 synthesis pellet compact. With a lower amount of Na<sub>2</sub>O<sub>2</sub>, the pellet is expected to undergo less disruption by cracking during the decomposition/reaction process which would result in greater conduction of internally generated heat to the surface of the pellet where temperatures are measured by pyrometer.

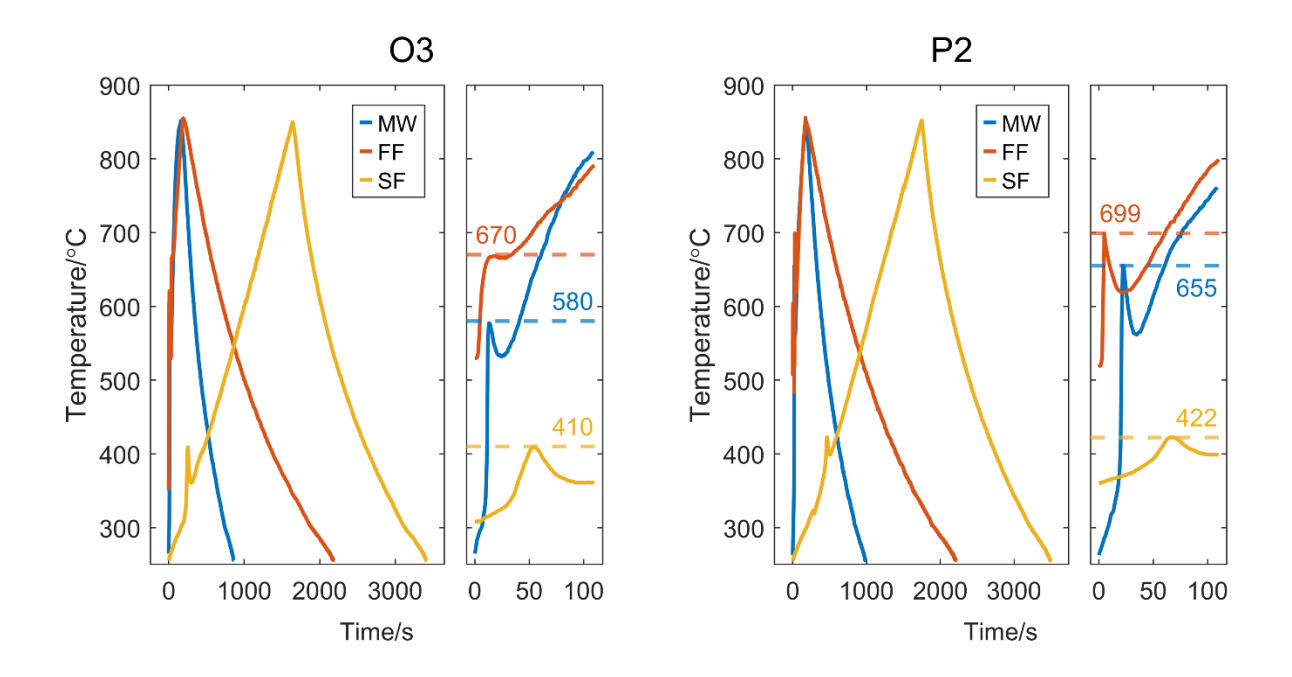


Figure 3: Temperature profiles of each method for the O3 synthesis (left) and P2 synthesis (right) as measured by optical pyrometer focused on the sample surface, where SF = "slow furnace", FF = "fast furnace", and MW = "microwave". Time = 0 indicates the first observation of temperatures >250 °C (gray line), which is the minimum temperature measurable by the optical pyrometer used in this study. The respective plot on the right of each show details of the reaction temperature spike (time is shifted to the onset of the temperature spike for comparison). Temperature profiles for the quenched intermediates can be found in the SI (SI A, Figure S1 and S2).

Table 4: O3 weight percent in the intermediates which were quenched immediately following initial reaction from starting material to products as determined by the occurrence of a temperature spike early in the heating process. Peak temperatures determined for the temperature spike are given. Weight fraction was determined by Rietveld analysis of the XRD data collected on the intermediates (SI C, Tables S9-14).

	•	O3 synthesis: Na:Co = $(1.05-1.10:1)$		P2 synthesis: Na:Co = (0.75-0.80:1)	
Intermediate O3 Method weight percent		Reaction peak temperature	Intermediate O3 weight percent	Reaction peak temperature	
MW	88%	564 °C	41%	639 °C	
FF	91%	657 °C	69%	724 °C	
SF	49%	399 °C	53%	438 °C	

After the initial exothermic reaction observed in all three cases, the phase fractions clearly diverge upon further heating directed by the precursor ratio: Na:Co = 0.75-0.80:1 results in a P2 type material whereas Na:Co = 1.05-1.10:1 results in a O3 type material. This suggests that the excess phase present at this intermediate stage of the reaction is extremely important in directing the subsequent phase conversions; i.e. either small excess of  $Co_3O_4$  in the 0.75:1 synthesis after initial reaction due to the Na deficiency relative to the average x in the Na<sub>x</sub>CoO<sub>2</sub> intermediate mixture, or larger excess of Na (likely in the form of Na<sub>2</sub>O<sub>2</sub> or Na<sub>2</sub>O) in the 1.05:1 synthesis due to the Na excess relative the average x in crystalline phase fraction (SI C, Table S9-14).

The micromorphology of the final products is very similar with respect to the heating method as shown by the SEM micrographs (Figure 4). As can be observed, these are significantly larger than the intermediates due to the agglomeration and growth of particles during the full heat treatment. The P2 type compounds exhibit irregular hexagonal plate morphology with particle sizes of  $\sim 1-5 \mu m$ . The O3 type product exhibits a thicker and more icosahedral morphology with larger particles of ~2–15 µm in size. The smaller particle size of the P2 product can be attributed to the nucleation-growth phase transition mechanism of 3-layer to 2-layer as suggested by Bianchini et al.<sup>9</sup> A significant difference in particle size is observed in the intermediates, however, where rapid heating methods (FF and MW) resulted in significantly larger particles relative to the slow furnace (SF) method. It is observed that the fast methods reach a much higher peak temperature at the time of the reaction and are quenched from a higher temperature (SI A, Figure S1-2, Table S1). It can be speculated that the agglomeration and growth process is significantly accelerated by the higher temperature reached. Because the higher "reaction peak" temperature is observed in both fast furnace and microwave methods this is likely purely a consequence of heating rate and any direct contribution of microwave irradiation is probably small.

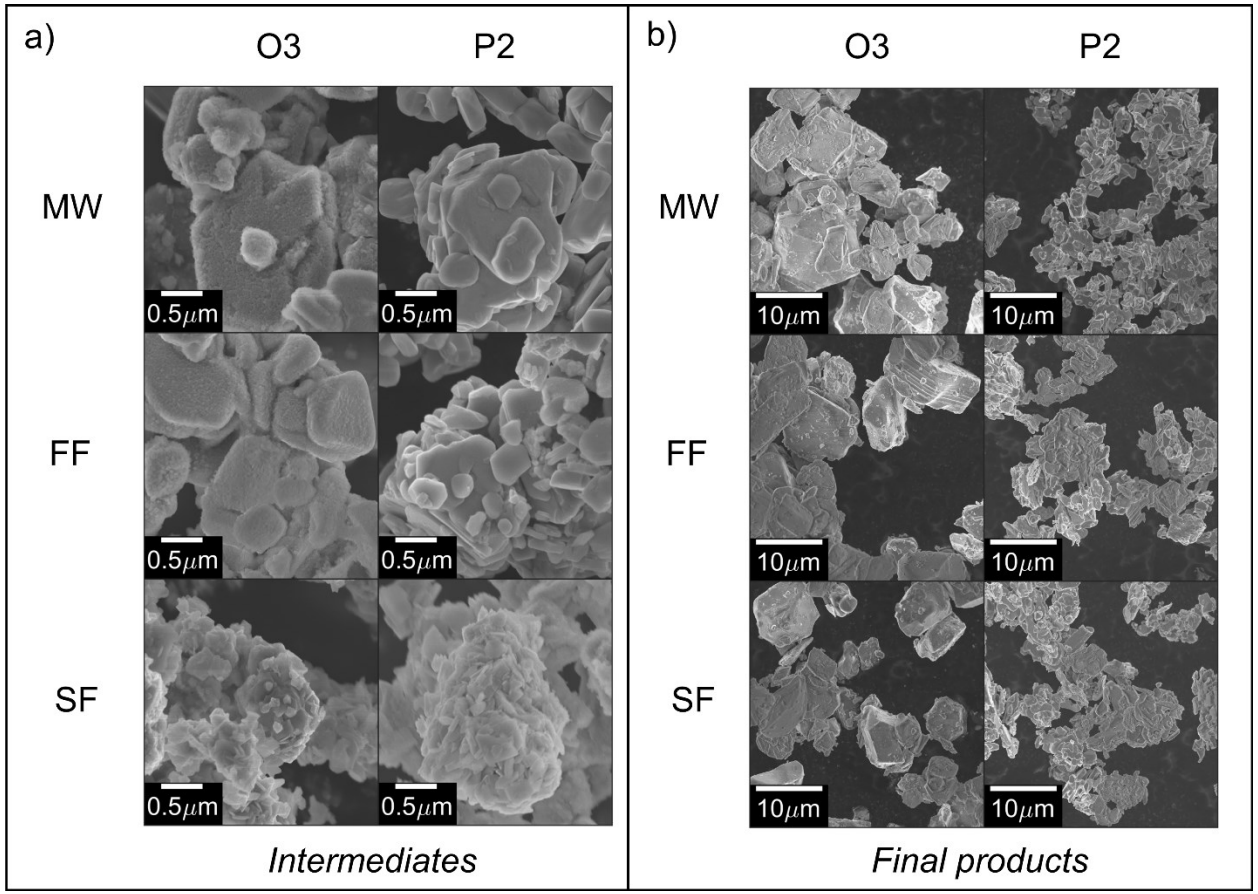


Figure 4: SEM micrographs of the quenched intermediates (a) and final products (b) for the different heating methods utilized. In each tile, the left column is the O3 syntheses, and the right column is the P2 syntheses. From top to bottom, these are synthesized by the MW, FF, and SF methods, respectively. The respective XRD data are shown in SI C, Figure S9-14 and Figure 2 for the intermediates and final products, respectively.

Room temperature Raman spectra were collected of the intermediates and the final products (Figure 5). Two Raman active modes are predicted ( $A_{1g} + E_{g}$ ) for the  $R\overline{3m}$  (166) space group of the O3 phase.<sup>39</sup> These have been observed experimentally by Yang *et al.*<sup>40</sup> as summarized in Table 5. Five Raman active modes are predicted ( $A_{1g} + E_{1g} + 3E_{2g}$ ) for the  $P6_{3}/mmc$  (194) space group of the P2 phase.<sup>41</sup> These were calculated by Li *et al.*<sup>42</sup> for the P2 phase using full or half sodium occupation (Table 6). Only the  $A_{1g}$ , one  $E_{2g}$ , and the  $E_{1g}$  modes have been observed experimentally for the P2 phase in polycrystalline samples<sup>41,43</sup> due to low Raman scattering intensity of the other modes as summarized in Table 6. This is attributed to disorder in the Na ions in this nonstoichiometric phase<sup>41</sup> and the lower optical skin depth for this metallic phase<sup>39</sup>. For the

O3 products, we observed two strong sharp Raman signals at 490-491 cm<sup>-1</sup> (E<sub>g</sub>) and 591-592 cm<sup>-1</sup> <sup>1</sup> (A<sub>1g</sub>). Raman signals were extremely weak and broad in the spectra of the P2 final products at  $460-464 \text{ cm}^{-1}(A_{1g})$  and  $583 \text{ cm}^{-1}(E_{1g})$ . These are somewhat lower in energy than those calculated by Li et al. 38 and those observed experimentally (Table 6). The large line width of the P2 type Raman signals (SI B, Table S2) at room temperature in general is attributed to disorder in the Na site occupancy, which is absent in the fully occupied O3-NaCoO<sub>2</sub> material.<sup>41</sup> We did not attempt to identify the E<sub>2g</sub> mode due to the low intensity of the spectra obtained. This mode may contribute to a lowered energy and larger line width of the overlapping A<sub>1g</sub> mode in our analysis. Lemmens et al.41 did not include this mode in their analysis either, yet their observation is significantly higher in energy (598 cm<sup>-1</sup>) for the A<sub>1g</sub> mode. In the intermediates, the Na<sub>x</sub>CoO<sub>2</sub> signals were closest to those of the O3 phase, with significant broadening only observed in those obtained from the SF method. This can be attributed to size related broadening<sup>44</sup> as the crystallite size is observed to be significantly smaller in the SEM images (Figure 4). In the SF method for both syntheses, an additional signal assigned to Co<sub>3</sub>O<sub>4</sub> (694 cm<sup>-1</sup>)<sup>45</sup> was observed, indicating significant Co<sub>3</sub>O<sub>4</sub> of high crystallinity persists and the reaction is not fully complete after the observation of the temperature spike indicating reaction of the precursors.

Na<sub>2</sub>CO<sub>3</sub> is a common impurity phase encountered when excess Na<sub>2</sub>O reacts with atmospheric CO<sub>2</sub>. The Raman Na<sub>2</sub>CO<sub>3</sub> peaks (1079 cm<sup>-1</sup>, 1083 cm<sup>-1</sup>)<sup>46</sup> are extremely small in the O3 type products and not detectable in the P2 type, despite its high Raman scattering intensity. The XRD refinement shows low Na<sub>2</sub>CO<sub>3</sub> in the MW O3 (2.0 wt.%) and SF O3 (1.6 wt.%) samples (SI C Tables S3, S5). All the P2 samples contain low amounts of Na<sub>2</sub>CO<sub>3</sub> with MW P2 (1.4 wt.%), FF P2 (1.6 wt.%), SF P2 (2.7 wt.%) (SI C Tables S6-8). No needle-like crystals characteristic of Na<sub>2</sub>CO<sub>3</sub> were visible in the SEM images (Figure 4).

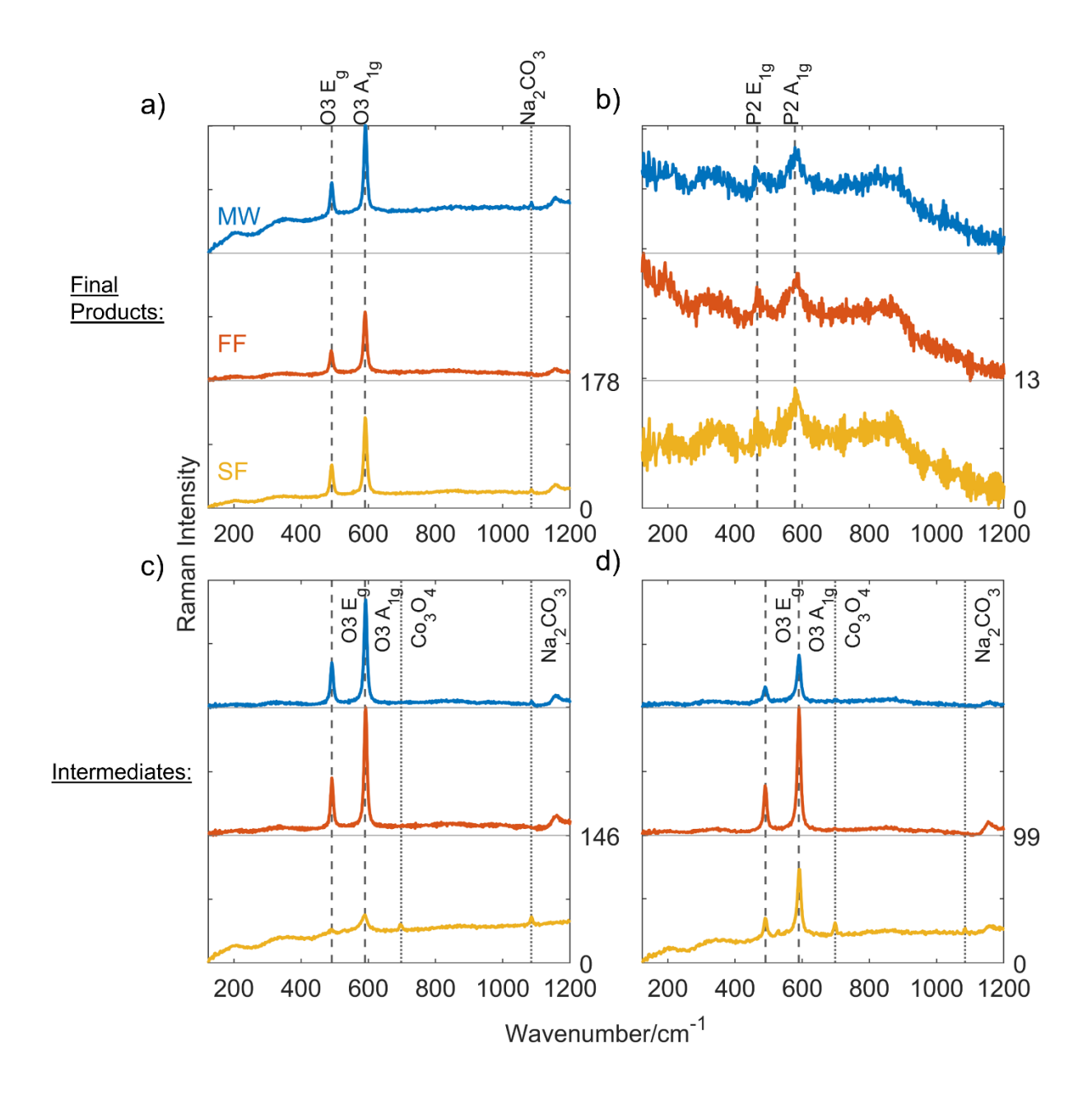


Figure 5: Room temperature Raman spectra of the final products (a and b are for O3 and P2 synthesis, respectively) and the intermediates (c and d are for O3 and P2 synthesis, respectively). Spectra within each graph are plotted on the same range of Raman intensity, shown at right for the bottom spectrum. Dashed vertical lines indicate identified Raman modes for  $Na_xCoO_2$ , while dotted lines indicate identified side phases.

Table 5: Experimentally observed modes in O3 as reported by Yang et al.<sup>40</sup>, and observed modes in this study for O3 products.

O3 Raman modes						
	(cm <sup>-1</sup> )					
Mode	Experimental <sup>40</sup>	This study				
$E_{g}$	486.5	490-491				
$A_{1g}$	586.4	591-592				

Table 6: Predicted Raman modes for P2 by Li *et al.*<sup>37</sup>, experimentally observed modes in P2 by Qu *et al.*<sup>43</sup> (a) and Lemmens *et al.*<sup>41</sup> (b), and observed modes in this study for P2 phase.

P2 Raman modes						
Mode	(cm <sup>-1</sup> )  Mode Predicted <sup>37</sup> Predicted <sup>37</sup> Experimental (a <sup>43</sup> , b <sup>41</sup> ) This study					
x in Na <sub>x</sub> CoO <sub>2</sub>	$\mathbf{x} = 1$	x = 0.5	x = 0.7	x = 0.68 - 0.76		
$E_{2g}$	172.9	185.7	-	-		
$\mathrm{E}_{1\mathrm{g}}$	477.1	482.1	$478.0^{\rm a}, 480^{\rm b}$	460-464		
$E_{2g}$	483.7	489.8	528.8a	-		
$A_{1g}$	608.0	604.6	585.5 <sup>a</sup> , 598 <sup>b</sup>	583		

Raman spectra were also collected in situ during the synthesis for the SF and MW methods (Figure 6). These results confirm that the initial formation of  $Na_xCoO_2$  occurs when the temperature spikes at ~350 °C. In both O3 and P2 syntheses,  $Na_xCoO_2$  signals, likely predominantly arising from the high intensity O3 phase Raman scattering, appear immediately following the disappearance of the signals assigned to  $Co_3O_4$  Raman scattering (SI G, Figure S25-28). Upon further heating, in the P2 synthesis these  $Na_xCoO_2$  signals gradually disappear, while in the O3 syntheses the signals grow in strength. The observation in the room temperature Raman spectra that the P2 phase has very small Raman scattering intensities confirms that the expected O3/O'3/P'3  $\rightarrow$  P2 conversion occurs following the initial first reaction in the P2 synthesis upon further heating. After the initial reaction, the secondary phase is  $Co_3O_4$  and the synthesis is directed to nucleation of the P2 phase in support of previous in situ study of the P2 synthesis by Bianchini et al. By Contrast, in the O3 syntheses, the transformation from O3/O'3  $\rightarrow$  O3 is observed instead. This demonstrates the secondary phase of  $Na_2O$  in O3 synthesis directs the phase transition of O'3

to O3. In light of previous investigation by Lei *et al.*<sup>7</sup> of the Na:Co and temperature solid-state synthesis phase diagram, where long holding times at lower temperatures (450 °C) were used to obtain the O3 phase, this indicates that the initial Na:Co ratio serves as a determining parameter. However, the temperature necessary to achieve the desired conversion is balanced by the time at temperature in the synthesis, indicating a highly dynamic process where kinetics must be considered in the O3 synthesis. Evidence for surface formation of Na<sub>2</sub>CO<sub>3</sub> is also observed with gradually strengthening signal intensity throughout both syntheses due to the expected reaction of Na<sub>2</sub>O with atmospheric CO<sub>2</sub> to form Na<sub>2</sub>CO<sub>3</sub>. However, the total amount produced appears low, as upon grinding and re-pelletizing the products, the signal intensity is greatly reduced in the room temperature spectra (Figure 5) and low weight fractions found in the XRD analysis (SI C Tables S3-8). Overall, no differences in the reaction pathway of O3 and P2 syntheses were observed between the furnace and microwave heating processes. Please note that defects in the Na<sub>x</sub>CoO<sub>2</sub> compounds can have an influence on the formation pathway, however, this goes beyond the scope of this study.

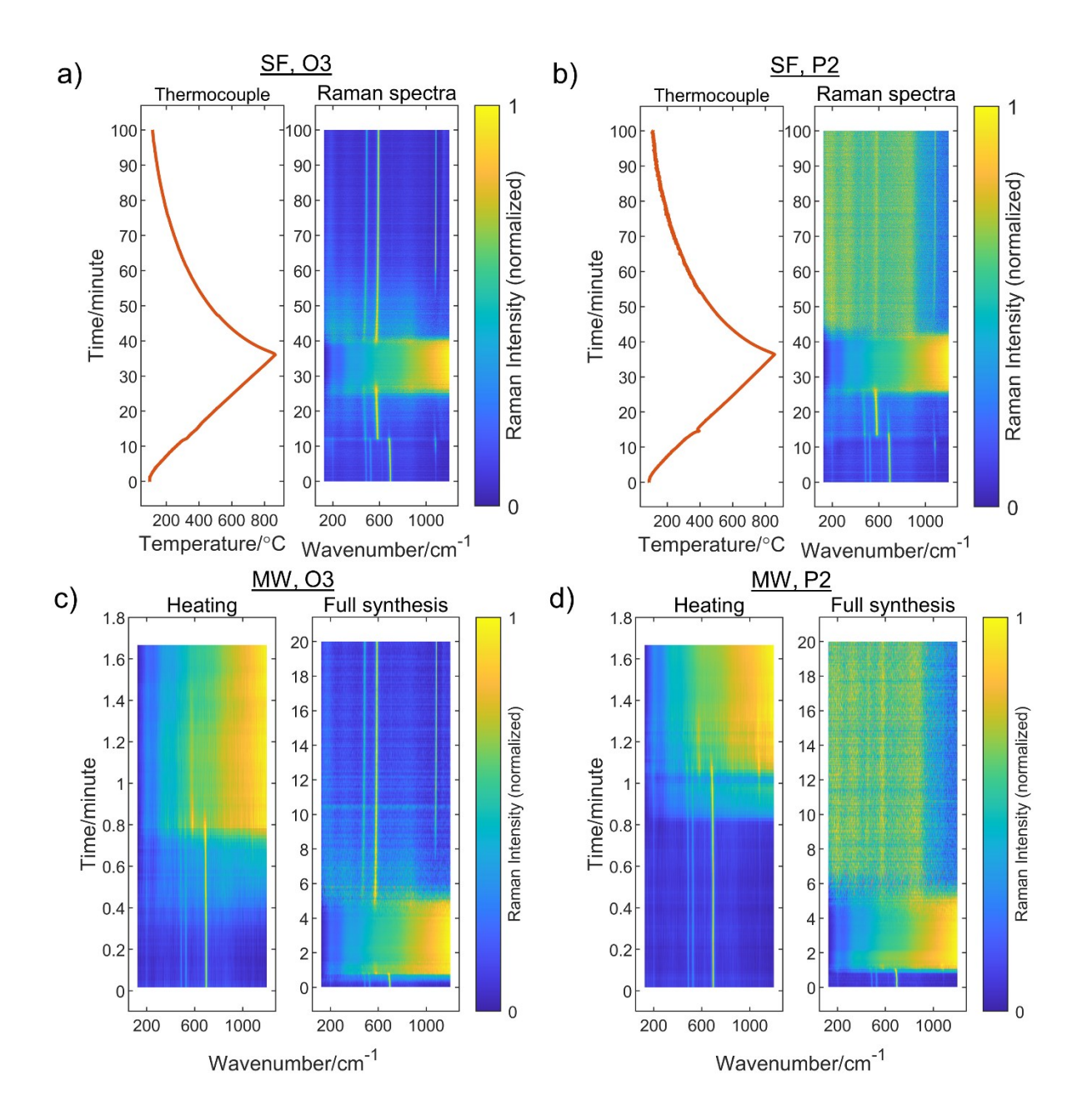


Figure 6: In situ Raman spectroscopy data collected during the Na<sub>x</sub>CoO<sub>2</sub> synthesis process by the slow furnace (SF) and microwave (MW) method. Temperature data in the SF methods were collected by a thermocouple placed on top of the sample surface. In the MW methods, no temperature data could be collected by thermocouple due to the microwave irradiation's damage potential. In these, the left plots instead show an expanded view of the heating process as the heating rates encountered were much larger. a) SF, O3; b) SF, P2; c) MW, O3; d) MW, P2. In all plots, the large broad intensity appearing at wavenumbers at high temperature is the result of thermal related background, which masks the signals at these temperatures.

We compared the electrochemical performance of cells containing P2 or O3 cathodes that were synthesized by the three heating methods. The representative galvanostatic charge/discharge

profiles are displayed in Figure 7 within the voltage range of 2.0–4.0 V vs. Na/Na<sup>+</sup>. Additional measurements are included in the SI D (Figure S15-18). Table 7 summarizes average initial discharge capacities. O3-NaCoO<sub>2</sub> prepared via MW, FF, and SF methods deliver the average initial discharge capacities (std. deviation) of 108.7 (0.7), 118.3 (1.5), and 114.0 (0.7) mAh g<sup>-1</sup>, respectively, at the current rate of 0.1C (Figure 7a). The capacities of those materials synthesized by the three different methods are lower than the >140 mAh g<sup>-1</sup> previously reported<sup>34</sup> at 0.05C, which could be attributed to the presence of impurity phases or the higher 0.1C rate used here. When the current increases to 1C, O3-NaCoO<sub>2</sub> synthesized via MW, FF, and SF methods experiences a slight decrease in average initial discharge capacities (std. deviation) of 89.4 (3.3), 96.6 (2.4), and 92.2 (3.6) mAh g<sup>-1</sup> (Figure 7c).

Correspondingly, P2-Na<sub>0.68-0.76</sub>CoO<sub>2</sub> synthesized via MW, FF, and SF methods deliver average initial discharge capacities (std. deviation) of 98.2 (0.1), 99.1 (1.8), and 92.3 (1.2) mAh g<sup>-1</sup>, respectively, at the current rate of 0.1C (Figure 7b). Their capacities are slightly lower than the previously reported capacity of 107 mAh g<sup>-1</sup> at 0.1C.<sup>35</sup> Under an increased rate of 1C, P2-Na<sub>0.7</sub>CoO<sub>2</sub> synthesized via MW, FF, and SF methods demonstrate average initial discharge capacities (std. deviation) of 73.2 (10.1), 61.8 (7.9), and 70.8 (22.0) mAh g<sup>-1</sup> (Figure 7d). The high standard deviation in the SF P2 sample is largely attributed to a large initial capacity for one measurement, 95.2 mAh g<sup>-1</sup>, whereas the other two measurements were 64.8 and 52.5 mAh g<sup>-1</sup>. The origin of this inconsistency is unknown.

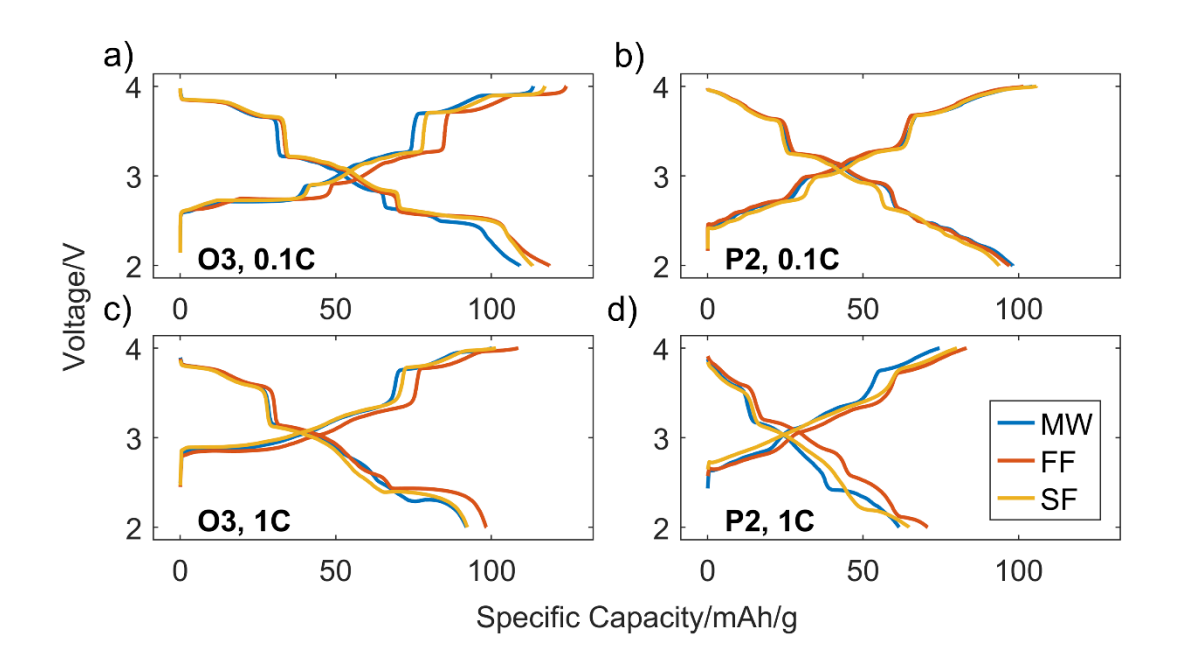


Figure 7: Charge/discharge profiles of the cells containing different P2/O3 cathodes countered with Na metal in 0.5 M NaClO<sub>4</sub> dissolved in PC (propylene carbonate) as the electrolyte within the voltage range of 2.0–4.0 V vs. Na/Na<sup>+</sup>. a-b) 2<sup>nd</sup> cycle at 0.1C, c-d) 3<sup>rd</sup> cycle at 1C charge rate with the activation cycles at 0.2C for the first 2 cycles, for O3 samples.

Table 7: Summary of the average initial discharge capacities and capacity retention. Average initial capacities at indicated rates (2<sup>nd</sup> cycle for 0.1C, 3<sup>rd</sup> cycle for 1C charged at 0.2C for 2 cycles) and standard deviations for three measurements from each heating method. Those reported by Yoshida *et al.* for O3 phase<sup>34</sup> and Ding *et al.* for P2 phase<sup>35</sup> are included for comparison. Average capacity retention after 100 cycles for 1C charge rate and standard deviations for three measurements.

Specific capacities: mAh g <sup>-1</sup> (std. deviation) Capacity retention % 100 cyles (std. deviation)							
Phase							
O3-NaCoO <sub>2</sub>	0.05C	>140 <sup>34</sup>					
	0.1C		108.7 (0.7)	118.3 (1.5)	114.0 (0.7)		
	1C		89.4 (3.3) 84.4% (12.5)	96.6 (2.4) 85.2% (18.2)	92.2 (3.6) 98.5% (4.9)		
P2-Na <sub>x</sub> CoO <sub>2</sub>	0.1C	107 <sup>35</sup>	98.2 (0.1)	99.1 (1.8)	92.3 (1.2)		
	1C		73.2 (10.1) 66.4% (62.0)	61.8 (7.9) 37.4% (9.3)	70.8 (22.0) 46.6% (53.7)		

The cycling stability and Coulombic efficiency of the corresponding cells at 1C over 100 cycles for one measurement are illustrated in Figure 8 (all three measurements are presented in the SI D, Figures S19 and S20). These values are summarized in Table 7, which includes the average

capacity and standard deviation of percent retention. At 1 C rate, O3-NaCoO<sub>2</sub> synthesized via MW, FF, and SF methods exhibit average capacity retentions (standard deviation) of 84.4% (12.5), 85.2% (18.2), and 98.5% (4.9), respectively. The high standard deviation in the FF O3 sample is attributed to one measurement which was significantly lower, 64.3%, than the other two, 97.4% and 94.0%.

For the P2-Na<sub>0.68-0.76</sub>CoO<sub>2</sub> samples at 1C, these samples synthesized via MW, FF, and SF methods have average capacity retentions (standard deviation) of 66.4% (62.0), 37.4% (9.3), and 46.6% (53.7), respectively (Figure 8b). Clearly, capacity retention characterization is inconsistent with the MW and SF methods. This is attributed to a dramatic capacity loss which is observed within 100 cycles only for two of the three measurements with these samples. The FF method instead shows this capacity loss consistently within 100 cycles for all three measurements.

In general, O3-NaCoO<sub>2</sub> displays better cyclability at 1C rate compared with P2-Na<sub>0.68-0.76</sub>CoO<sub>2</sub>, which might be attributed to their larger lattice parameters, facilitating sodium ion intercalation despite their larger particle size. By contrast, the capacity of P2-Na<sub>0.68-0.76</sub>CoO<sub>2</sub> is not directly correlated with lattice parameters, and their rapid capacity loss might be related to the structure stability, which can be influenced by many other factors. These understandings are beyond the scope of this study.

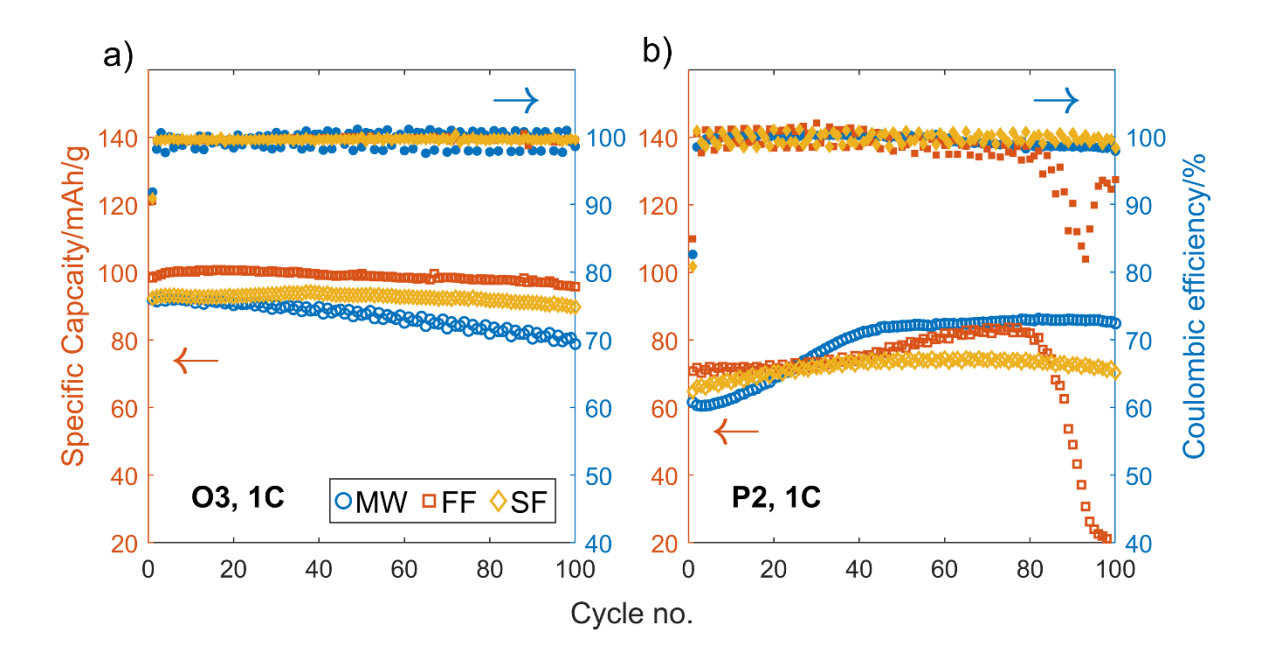


Figure 8: Cycling stability of the O3/P2 cathodes at 1C during 3–102 cycles within the voltage range of 2.0–4.0 V vs Na/Na<sup>+</sup>, the cells were activated at 0.2C for the first two cycles. a) O3 type samples b) P2 type samples.

# **CONCLUSIONS**

In this study, O3 type NaCoO<sub>2</sub> and P2 type Na<sub>0.68-0.76</sub>CoO<sub>2</sub> were successfully prepared using rapid microwave heating. The structure, morphology, and battery performance of these products were compared to those obtained by furnace heating where we compared high to low heating rates. No significant differences were found in structure or morphology, though phase purity of the O3 phase was slightly lower with microwave heating. Battery performance showed similar initial capacities regardless of the synthesis method, but rapid capacity fading in some P2 phase measurements suggested short-range structure defects from fast heating. The formation processes of both compounds were examined using our home-built in situ Raman spectroscopy setup as well as ex situ powder diffraction and electron microscopy. In all methods, 3-layer polytypes formed initially, with faster heating accelerating the initial reaction and resulting in larger grain sizes. The final phase (O3 or P2) was determined by the initial Na precursor ratio. In

situ Raman data showed no differences in synthesis pathways between heating methods. This study demonstrates that microwave heating is a viable alternative for synthesizing Na<sub>x</sub>CoO<sub>2</sub> materials with similar characteristics to those produced by traditional methods.

# **Supporting Information.**

Additional pyrometer temperature data, room-temperature Raman spectra peak analysis, Rietveld refinements of the XRD data, battery measurements for individual samples, instrument modifications, XRD data for lower synthesis temperatures, selected Raman spectra from in situ data.

NaxCoO2 MW SupportingInformation.docx

#### **AUTHOR INFORMATION**

# **Corresponding Author**

Christina Birkel, christina.birkel@asu.edu

### **Author Contributions**

J. Jamboretz contributed all synthesis, measurement, and analysis of the samples except battery measurements and wrote the manuscript except battery related discussion. Y. Zhu contributed the battery measurements and analysis and wrote battery related discussion. R. James contributed to the development of synthesis methods. C. S. Birkel provided the research question, edited, and reviewed the manuscript. L. Mu supervised the battery analysis and edited and reviewed the manuscript.

# **Funding Sources**

This material is based upon work supported by the National Science Foundation under Grant No. 2143982.

#### **ACKNOWLEDGMENT**

We acknowledge the use of facilities within the Eyring Materials Center at Arizona State University supported in part by NNCI-ECCS-1542160.

### **ABBREVIATIONS**

SIB: Sodium ion battery

O3: NaCoO<sub>2</sub> with O3 type structure by Delmas notation.

O'3: Na<sub>0.83</sub>CoO<sub>2</sub> with O'3 type structure by Delmas notation.

P'3: Na<sub>0.60</sub>CoO<sub>2</sub> with P'3 type structure by Delmas notation.

P2: Na<sub>0.68-0.76</sub>CoO<sub>2</sub> with P2 type structure by Delmas notation.

MW: Microwave heating method.

FF: Fast furnace heating method.

SF: Slow furnace heating method.

XRD: X-Ray Diffraction

SEM: Scanning Election Microscopy

PVDF: polyvinylidene fluoride

NMP: N-methyl-2-pyrrolidone

#### REFERENCES

- (1) Komaba, S.; Kubota, K. Layered NaMO<sub>2</sub> for the Positive Electrode. In *Na-ion Batteries*; John Wiley & Sons, Ltd, 2021; pp 1–46. https://doi.org/10.1002/9781119818069.ch1.
- (2) Liu, Q.; Hu, Z.; Chen, M.; Zou, C.; Jin, H.; Wang, S.; Chou, S.; Dou, S. Recent Progress of Layered Transition Metal Oxide Cathodes for Sodium-Ion Batteries. *Small* **2019**, *15* (32). https://doi.org/10.1002/smll.201805381.
- (3) Gao, R.-M.; Zheng, Z.-J.; Wang, P.-F.; Wang, C.-Y.; Ye, H.; Cao, F.-F. Recent Advances and Prospects of Layered Transition Metal Oxide Cathodes for Sodium-Ion Batteries. *Energy Storage Mater.* **2020**, *30*, 9–26. https://doi.org/10.1016/j.ensm.2020.04.040.
- (4) Su, H.; Jaffer, S.; Yu, H. Transition Metal Oxides for Sodium-Ion Batteries. *Energy Storage Mater.* **2016**, *5*, 116–131. https://doi.org/10.1016/j.ensm.2016.06.005.
- (5) Delmas, C.; Fouassier, C.; Hagenmuller, P. Structural Classification and Properties of the Layered Oxides. *Phys. BC* **1980**, *99* (1–4), 81–85. https://doi.org/10.1016/0378-4363(80)90214-4.

- (6) Guo, S.; Sun, Y.; Yi, J.; Zhu, K.; Liu, P.; Zhu, Y.; Zhu, G.; Chen, M.; Ishida, M.; Zhou, H. Understanding Sodium-Ion Diffusion in Layered P2 and P3 Oxides via Experiments and First-Principles Calculations: A Bridge between Crystal Structure and Electrochemical Performance. NPG Asia Mater. 2016, 8 (4), e266–e266. https://doi.org/10.1038/am.2016.53.
- (7) Lei, Y.; Li, X.; Liu, L.; Ceder, G. Synthesis and Stoichiometry of Different Layered Sodium Cobalt Oxides. *Chem. Mater.* **2014**, *26* (18), 5288–5296. https://doi.org/10.1021/cm5021788.
- (8) Berthelot, R.; Carlier, D.; Delmas, C. Electrochemical Investigation of the P2-Na<sub>x</sub>CoO<sub>2</sub> Phase Diagram. *Nat. Mater.* **2011**, *10* (1), 74–80. https://doi.org/10.1038/nmat2920.
- (9) Bianchini, M.; Wang, J.; Clément, R. J.; Ouyang, B.; Xiao, P.; Kitchaev, D.; Shi, T.; Zhang, Y.; Wang, Y.; Kim, H.; Zhang, M.; Bai, J.; Wang, F.; Sun, W.; Ceder, G. The Interplay between Thermodynamics and Kinetics in the Solid-State Synthesis of Layered Oxides. *Nat. Mater.* **2020**, *19* (10), 1088–1095. https://doi.org/10.1038/s41563-020-0688-6.
- (10) Siebert, J. P.; Hamm, C. M.; Birkel, C. S. Microwave Heating and Spark Plasma Sintering as Non-Conventional Synthesis Methods to Access Thermoelectric and Magnetic Materials. *Appl. Phys. Rev.* **2019**, *6* (4), 041314. https://doi.org/10.1063/1.5121442.
- (11) Kitchen, H. J.; Vallance, S. R.; Kennedy, J. L.; Tapia-Ruiz, N.; Carassiti, L.; Harrison, A.; Whittaker, A. G.; Drysdale, T. D.; Kingman, S. W.; Gregory, D. H. Modern Microwave Methods in Solid-State Inorganic Materials Chemistry: From Fundamentals to Manufacturing. *Chem. Rev.* **2014**, *114* (2), 1170–1206. https://doi.org/10.1021/cr4002353.
- (12) Levin, E. E.; Grebenkemper, J. H.; Pollock, T. M.; Seshadri, R. Protocols for High Temperature Assisted-Microwave Preparation of Inorganic Compounds. *Chem. Mater.* **2019**, 31 (18), 7151–7159. https://doi.org/10.1021/acs.chemmater.9b02594.
- (13) Horikoshi, S.; Schiffmann, R. F.; Fukushima, J.; Serpone, N. *Microwave Chemical and Materials Processing*; Springer Singapore, 2018. https://doi.org/10.1007/978-981-10-6466-1 1.
- (14) Baghurst, D. R.; Mingos, D. M. P. Application of Microwave Heating Techniques for the Synthesis of Solid State Inorganic Compounds. *J. Chem. Soc. Chem. Commun.* **1988**, No. 12, 829. https://doi.org/10.1039/c39880000829.
- (15) Rao, K. J.; Vaidhyanathan, B.; Ganguli, M.; Ramakrishnan, P. A. Synthesis of Inorganic Solids Using Microwaves. *Chem. Mater.* **1999**, *11* (4), 882–895. https://doi.org/10.1021/cm9803859.
- (16) Siebert, J. P.; Patarakun, K.; Birkel, C. S. Mechanistic Insights into the Nonconventional Sol–Gel Synthesis of MAX Phase M<sub>2</sub>GeC (M = V, Cr). *Inorg. Chem.* **2022**, *61* (3), 1603–1610. https://doi.org/10.1021/acs.inorgchem.1c03415.
- (17) Hamm, C. M.; Schäfer, T.; Zhang, H.; Birkel, C. S. Non-conventional Synthesis of the 413 MAX Phase V<sub>4</sub>AlC<sub>3</sub>. *Z. Für Anorg. Allg. Chem.* **2016**, *642* (23), 1397–1401. https://doi.org/10.1002/zaac.201600370.
- (18) Mingos, D. M. P.; Baghurst, D. R. Tilden Lecture. Applications of Microwave Dielectric Heating Effects to Synthetic Problems in Chemistry. *Chem. Soc. Rev.* **1991**, *20* (1), 1–47. https://doi.org/10.1039/CS9912000001.
- (19) Yang, G.; Kong, Y.; Hou, W.; Yan, Q. Heating Behavior and Crystal Growth Mechanism in Microwave Field. *J. Phys. Chem. B* **2005**, *109* (4), 1371–1379. https://doi.org/10.1021/jp0470905.
- (20) Subramanian, V.; Chen, C. L.; Chou, H. S.; Fey, G. T. K. Microwave-Assisted Solid-State Synthesis of LiCoO<sub>2</sub> and Its Electrochemical Properties as a Cathode Material for Lithium Batteries. *J. Mater. Chem.* **2001**, *11* (12), 3348–3353. https://doi.org/10.1039/b105008g.

- (21) Nakayama, M.; Watanabe, K.; Ikuta, H.; Uchimoto, Y.; Wakihara, M. Grain Size Control of LiMn<sub>2</sub>O<sub>4</sub> Cathode Material Using Microwave Synthesis Method. *Solid State Ion.* **2003**, *164* (1–2), 35–42. https://doi.org/10.1016/j.ssi.2003.08.048.
- (22) Mastrovito, C.; Lekse, J. W.; Aitken, J. A. Rapid Solid-State Synthesis of Binary Group 15 Chalcogenides Using Microwave Irradiation. *J. Solid State Chem.* **2007**, *180* (11), 3262–3270. https://doi.org/10.1016/j.jssc.2007.09.001.
- (23) Lekse, J. W.; Stagger, T. J.; Aitken, J. A. Microwave Metallurgy: Synthesis of Intermetallic Compounds via Microwave Irradiation. *Chem. Mater.* **2007**, *19* (15), 3601–3603. https://doi.org/10.1021/cm0707410.
- (24) Lekse, J. W.; Pischera, A. M.; Aitken, J. A. Understanding Solid-State Microwave Synthesis Using the Diamond-like Semiconductor, AgInSe<sub>2</sub>, as a Case Study. *Mater. Res. Bull.* **2007**, 42 (3), 395–403. https://doi.org/10.1016/j.materresbull.2006.09.025.
- (25) Biswas, K.; Muir, S.; Subramanian, M. A. Rapid Microwave Synthesis of Indium Filled Skutterudites: An Energy Efficient Route to High Performance Thermoelectric Materials. *Mater. Res. Bull.* **2011**, 46 (12), 2288–2290. https://doi.org/10.1016/J.MATERRESBULL.2011.08.058.
- (26) Muir, S. W.; Rachdi, O. D.; Subramanian, M. A. Rapid Microwave Synthesis of the Iron Arsenides NdFeAsO and NdFe<sub>0.9</sub>Co<sub>0.1</sub>AsO. *Mater. Res. Bull.* **2012**, *47* (3), 798–800. https://doi.org/10.1016/J.MATERRESBULL.2011.11.062.
- (27) Vaucher, S.; Stir, M.; Ishizaki, K.; Catala-Civera, J. M.; Nicula, R. Reactive Synthesis of Ti-Al Intermetallics during Microwave Heating in an E-Field Maximum. *Thermochim. Acta* **2011**, *522* (1–2), 151–154. https://doi.org/10.1016/j.tca.2010.11.026.
- (28) Vaucher, S.; Nicula, R.; Català-Civera, J. M.; Schmitt, B.; Patterson, B. In Situ Synchrotron Radiation Monitoring of Phase Transitions during Microwave Heating of Al-Cu-Fe Alloys. *J. Mater. Res.* **2008**, *23* (1), 170–175. https://doi.org/10.1557/jmr.2008.0009.
- (29) Vaucher, S.; Catala-Civera, J.-M.; Sarua, A.; Pomeroy, J.; Kuball, M. Phase Selectivity of Microwave Heating Evidenced by Raman Spectroscopy. *J. Appl. Phys.* **2006**, *99* (11), 113505. https://doi.org/10.1063/1.2198931.
- (30) Garcia-Baños, B.; Catalá-Civera, J.; Peñaranda-Foix, F.; Plaza-González, P.; Llorens-Vallés, G. In Situ Monitoring of Microwave Processing of Materials at High Temperatures through Dielectric Properties Measurement. *Materials* **2016**, *9* (5), 349. https://doi.org/10.3390/ma9050349.
- (31) García-Baños, B.; Reinosa, J. J.; Peñaranda-Foix, F. L.; Fernández, J. F.; Catalá-Civera, J. M. Temperature Assessment Of Microwave-Enhanced Heating Processes. *Sci. Rep.* **2019**, *9* (1), 10809. https://doi.org/10.1038/s41598-019-47296-0.
- (32) Günter, M. M.; Korte, C.; Brunauer, G.; Boysen, H.; Lerch, M.; Suard, E. In Situ High Temperature Neutron Diffraction Study of Sr/Mg-Doped Lanthanum Gallate Superionic Conductors under Microwave Irradiation. *Z. Anorg. Allg. Chem.* **2005**, *631* (6–7), 1277–1284. https://doi.org/10.1002/zaac.200500042.
- (33) Jamboretz, J.; Reitz, A.; Birkel, C. S. Development of a Raman Spectroscopy System for in Situ Monitoring of Microwave-assisted Inorganic Transformations. *J. Raman Spectrosc.* **2023**, *54* (3), 296–304. https://doi.org/10.1002/jrs.6478.
- (34) Yoshida, H.; Yabuuchi, N.; Komaba, S. NaFe<sub>0.5</sub>Co<sub>0.5</sub>O<sub>2</sub> as High Energy and Power Positive Electrode for Na-Ion Batteries. *Electrochem. Commun.* **2013**, *34*, 60–63. https://doi.org/10.1016/j.elecom.2013.05.012.

- (35) Ding, J. J.; Zhou, Y. N.; Sun, Q.; Yu, X. Q.; Yang, X. Q.; Fu, Z. W. Electrochemical Properties of P2-Phase Na<sub>0.74</sub>CoO<sub>2</sub> Compounds as Cathode Material for Rechargeable Sodium-Ion Batteries. *Electrochimica Acta* **2013**, 87, 388–393. https://doi.org/10.1016/j.electacta.2012.09.058.
- (36) Coelho, A. A. TOPAS and TOPAS-Academic: An Optimization Program Integrating Computer Algebra and Crystallographic Objects Written in C++. *J. Appl. Crystallogr.* **2018**, 51 (1), 210–218. https://doi.org/10.1107/S1600576718000183.
- (37) Takahashi, Y.; Gotoh, Y.; Akimoto, J. Single-Crystal Growth, Crystal and Electronic Structure of NaCoO<sub>2</sub>. *J. Solid State Chem.* **2003**, *172* (1), 22–26. https://doi.org/10.1016/S0022-4596(02)00042-7.
- (38) Viciu, L.; Huang, Q.; Cava, R. J. Stoichiometric Oxygen Content in Na<sub>x</sub>CoO<sub>2</sub>. *Phys. Rev. B* **2006**, 73 (21), 212107. https://doi.org/10.1103/PhysRevB.73.212107.
- (39) Inaba, M.; Iriyama, Y.; Ogumi, Z.; Todzuka, Y.; Tasaka, A. Raman Study of Layered Rock-Salt LiCoO<sub>2</sub> and Its Electrochemical Lithium Deintercalation. *J. Raman Spectrosc.* **1997**, *28* (8), 613–617. https://doi.org/10.1002/(SICI)1097-4555(199708)28:8<613::AID-JRS138>3.0.CO;2-T.
- (40) Yang, H. X.; Xia, Y.; Shi, Y. G.; Tian, H. F.; Xiao, R. J.; Liu, X.; Liu, Y. L.; Li, J. Q. Raman Spectroscopy Study of α-, β-, γ-Na<sub>x</sub>CoO<sub>2</sub> and γ-(Ca,Sr)<sub>x</sub>CoO<sub>2</sub>. *Phys. Rev. B Condens. Matter Mater. Phys.* **2006**, 74 (9), 94301. https://doi.org/10.1103/PhysRevB.74.094301.
- (41) Lemmens, P.; Gnezdilov, V.; Kovaleva, N. N.; Choi, K. Y.; Sakurai, H.; Takayama-Muromachi, E.; Takada, K.; Sasaki, T.; Chou, F. C.; Chen, D. P.; Lin, C. T.; Keimer, B. Effect of Na Content and Hydration on the Excitation Spectrum of the Cobaltite Na<sub>x</sub>CoO<sub>2</sub>·yH<sub>2</sub>O. *J. Phys. Condens. Matter* **2004**, *16* (11 SPEC. ISS.), S857--S865. https://doi.org/10.1088/0953-8984/16/11/041.
- (42) Li, Z.; Yang, J.; Hou, J. G.; Zhu, Q. First-Principles Lattice Dynamics of NaCoO<sub>2</sub>. *Phys. Rev. B Condens. Matter Mater. Phys.* **2004**, 70 (14), 144518. https://doi.org/10.1103/PhysRevB.70.144518.
- (43) Qu, J. F.; Wang, W.; Chen, Y.; Li, G.; Li, X. G. Raman Spectra Study on Nonstoichiometric Compound Na<sub>x</sub>CoO<sub>2</sub>. *Phys. Rev. B* **2006**, *73* (9), 092518. https://doi.org/10.1103/PhysRevB.73.092518.
- (44) Gouadec, G.; Colomban, P. Raman Spectroscopy of Nanomaterials: How Spectra Relate to Disorder, Particle Size and Mechanical Properties. *Prog. Cryst. Growth Charact. Mater.* **2007**, *53* (1), 1–56. https://doi.org/10.1016/j.pcrysgrow.2007.01.001.
- (45) Hadjiev, V. G.; Iliev, M. N.; Vergilov, I. V. The Raman Spectra of Co<sub>3</sub>O<sub>4</sub>. *J. Phys. C Solid State Phys.* **1988**, *21* (7), L199–L201. https://doi.org/10.1088/0022-3719/21/7/007.
- (46) Brooker, M. H.; Bates, J. B. Raman and Infrared Spectral Studies of Anhydrous Li<sub>2</sub>CO<sub>3</sub> and Na<sub>2</sub>CO<sub>3</sub>. *J. Chem. Phys.* **1971**, *54* (11), 4788–4796. https://doi.org/10.1063/1.1674754.

# "For Table of Contents Only"

